Present-Day Tropical Convection Determines Future Equatorial Pacific Temperature Trends

S. Stevenson[1*], C. Deser[2], S. Coats[3], G. Falster[4], B. Konecky[5], N. Maher[6,7], C. Pfleger[1]

[1]University of California, Santa Barbara, Santa Barbara, CA, USA
[2]National Center for Atmospheric Research, Boulder, CO, USA
[3]University of Hawaii at Manoa, Honolulu, HI, USA
[4]The University of Adelaide, Adelaide, SA, Australia
[5]Washington University of St Louis, St. Louis, MO, USA
[6]Australian National University, Canberra, ACT, Australia
[7]ARC Centre of Excellence for Weather of the 21st Century

*Corresponding author. Email: sstevenson@ucsb.edu

The equatorial Pacific sea surface temperature (SST) zonal gradient has worldwide impacts, and is expected to be highly sensitive to future climate change. However, biases in climate models call the reliability of future SST gradient projections into question. Here we combine multiple climate model Large Ensembles to show that equatorial precipitation and cloud feedbacks have a controlling influence on the future Pacific SST gradient. An 'SST Gradient Sensitivity' parameter is computed for each model, which shows that models with stronger historical equatorial precipitation have systematically higher sensitivities (more El Nino-like changes). This arises from the stronger negative SST-shortwave radiation feedback, which then creates a wind response that favors El Nino-like warming. Notably, when historical deep convection is sufficiently strong, a 'saturation' effect occurs that tends to inhibit this effect. These results imply that models likely underestimate future El Nino-like changes, but that the 'true' magnitude of changes may be predictable.

1 Introduction

The pattern of equatorial Pacific sea surface temperature (SST) is critically important for a variety of human and natural systems. The zonal SST contrast (SST gradient) along the equator is particularly impactful, since it is closely tied to the location of equatorial deep convection, which alters the propagation of atmospheric circulation anomalies and associated weather patterns around the world (*1, 2*). The equatorial Pacific SST gradient (hereafter, "SST gradient" or ΔSST) is expected to be strongly modified by ongoing anthropogenic climate change, but the overall magnitude and sign of this effect remains poorly understood (*3*). Therefore, it is critical to quantify the true sensitivity of the Pacific SST gradient to future human influences in order to improve future projections of climate change impacts.

Coupled climate models generally simulate a weakening of ΔSST in response to greenhouse gas (GHG) increases (*4*). Yet it is not clear whether this is an accurate representation of the real world as models have known biases in their simulation of equatorial Pacific climate (*5, 6*), which have been suggested to affect the sensitivity of SST patterns to warming (*7–9*). Additionally, model simulations of the recent observational period (20th and early 21st centuries) are unable to reproduce the observed tendency for ΔSST strengthening (*10*). Internal climate variability likely contributes to this disagreement, yet recent work indicates that even after accounting for such effects, models are still highly unlikely to simulate the observed recent ΔSST strengthening (*11*).

One difficulty with assessing the accuracy of ΔSST trends in coupled models is our limited understanding of the balance of mechanisms governing their variability and change. Multiple hypotheses have been proposed for the influence of GHG emissions on ΔSST. These include thermodynamic responses in the atmosphere (*12*), the behavior of the oceanic subtropical cells (*13*), changes in mean atmospheric stability (*14*), and differences in the radiative sensitivity of SST across the basin (*15*), among others (see review by (*3*) for details). There is likely to be substantial structural uncertainty in the relative magnitudes of these various mechanisms, but separating structural uncertainty from other forms of uncertainty requires a large number of simulations. Until recently, a suite of simulations of sufficient size has not been available, making it more difficult to draw firm conclusions regarding the influence of model physics on ΔSST changes due to confounding effects from internal climate variability.

Here we address the question of ΔSST response to 21st century radiative forcing using a suite of 'Large Ensemble' (LE) simulations run with a variety of climate models (*16*). An LE is a set of simulations run with a single model, where all simulations are identical with the exception of their initial climate state (e.g. (*17*)). Over the past 10 years, LEs have been run with many different models, and have become widely used in the climate community to separate the forced response from internal variability (*18, 19*). These LEs now make it possible to directly and robustly examine the differences in models' forced responses to climate change (determined from the ensemble mean of each LE), and assess their causes. We note that all LEs analyzed here are members of the CMIP6 model generation (Table S1), which show a higher degree of consistency in the sign of ΔSST change relative to CMIP5 (*20, 21*). This choice was made in order to prevent complications from arising due to the known differences in climate sensitivity and the treatment of cloud microphysical processes between CMIP5 and CMIP6 models (*22, 23*).

2 SST Gradient Sensitivity

The overall response of ΔSST to various future emissions scenarios is summarized in Figure 1, where the gradient is defined as the difference between temperatures in the eastern and western equatorial Pacific (Methods). All LEs simulate a weakening of ΔSST over the 21st century, the magnitude of which tends to be larger for higher-emissions scenarios (e.g. compare values in Figure 1e across scenarios for a given model). However, for a given emissions scenario, the ΔSST change differs between LEs, suggesting a role for inter-model physical differences. For instance, the CESM2 has a much stronger response than other models to the SSP5-8.5 (Figure 1a), SSP3-7.0 (Figure 1b), and SSP2-4.5 (Figure 1c) scenarios. At the other end of the spectrum, the IPSL-CM6A exhibits almost no response to either SSP5-8.5 or SSP3-7.0 (the only two scenarios available for this model). There is also some notable non-monotonicity, primarily in the lower-emission scenarios: all three of the models which ran the SSP1-2.6 scenario level off in their responses between 2060-2100 (Figure 1d) and some indications of similar behavior can be seen under SSP2-4.5 by the end of the century (Figure 1c). ΔSST changes are summarized as epoch differences in Figure 1e, where it is immediately obvious that some models' zonal SST gradient is systematically more responsive to future climate change than others.

The model differences between projections of 21st century gradient changes become especially apparent when the ΔSST time series are normalized to their respective global-mean temperature increases (Figure 1f, Figure S1). Some models can then be easily distinguished in terms of their ΔSST sensitivity to global-mean temperature increases; for instance, CanESM5 and IPSL-CM6A exhibit little change, while models such as MIROC6 and CESM2 are especially responsive (Figure S1b). Interestingly, the *relative* magnitude of epoch changes in ΔSST is approximately constant across emissions scenarios for many models (Figure 1f). One exception is the CESM2, where the response to SSP3-7.0 forcing is proportionally smaller than the response to the other two scenarios. We speculate that this may be related to CESM2's high climate sensitivity, which has been demonstrated to lead to strong and compensatory responses to GHG and aerosol emissions (*24*). Given that SSP3-7.0 has relatively high aerosol forcing (*25*), this might then create overly strong damping in CESM2. Nevertheless, it appears that generally speaking, the balance of mechanisms governing ΔSST change at the end of the 21st century does differ systematically between climate models, but remains relatively consistent across emissions scenarios for LEs run with a given model.

Using the results of Figure 1, we define an 'SST Gradient Sensitivity' parameter (hereafter Δ_Δ) to classify models according to their tropical Pacific responses. The Δ_Δ parameter is equal to the value of the change in ΔSST between the 20th century (1951-2000) and 21st century (2051-2100), normalized to the change in global-mean temperature over those same periods (Figure 1f). Where simulations with multiple emissions scenarios are available, these have been used to estimate a scenario-mean ΔSST sensitivity and associated uncertainty (Table S2); in subsequent analyses, the ΔSST sensitivities computed for individual model/scenario combinations are employed. The results are somewhat sensitive to the start and end points chosen, possibly due to the higher importance of aerosol forcing in the 20th/early 21st centuries (not pictured) - here we use the latter halves of the 21st and 20th centuries, to more clearly isolate the effect of greenhouse gas emissions (Methods). To provide some validation of the relative magnitudes of the Δ_Δ parameters, we also compute the linear trend in ΔSST over 1950-2100 normalized to the linear trend in global-mean temperature and average over all scenarios available for a given model (Table S3). This shows qualitatively similar results to the Δ_Δ defined using epoch differences.

3 Future Changes Associated with SST Gradient Sensitivity

To investigate the mechanisms driving differences in Δ_Δ, we apply an ensemble-mean correlation analysis. This relates the ensemble mean Δ_Δ for a given model and a given scenario to that ensemble's underlying mean climatological patterns of air temperature, precipitation, and other key variables (Figure 2). For example, for each model/scenario combination, the ensemble mean Δ_Δ is calculated, then correlated at each grid point with that grid point's historical mean air temperature (Figure 2a) or that grid point's future change in mean air temperature (Figure 2b). In addition to surface air temperature, the ensemble mean Δ_Δ was regressed against grid point SLP, precipitation, and geopotential height. The resulting Pearson's correlation coefficient (r) reveals, for the full set of model/scenario combinations, the overall patterns of temperature and atmospheric circulation associated with inter-model differences in Δ_Δ.

Figure 2 shows that there is a spatially coherent pattern of future changes associated with the ensemble-mean Δ_Δ. By construction, warming in the eastern equatorial Pacific is present, along with cooling over the western Pacific warm pool (Figure 2b). However, ΔSST reductions are also associated with other regions: future warming in the North Pacific, the tropical Atlantic, and the North American continent are associated with El Niño-like changes (Figure 2b). The future precipitation changes associated with ΔSST reductions (Figure 2d) include an overall reduction in precipitation north of the equator throughout the central/eastern Pacific, and a dipolar precipitation signal in the Indian Ocean and tropical Atlantic. In the Northern Hemisphere midlatitudes, the 500 hPa geopotential height changes include low heights over the Atlantic and much of Eurasia (Figure 2d). In contrast, the Southern Hemisphere midlatitude circulation exhibits more zonal structure, with lows over Australia and South America coincident with local surface cooling (Figure 2d).

To determine the degree to which the associations in Figure 2 are representative of overall coherent inter-model spread patterns, we also calculate the EOF modes of ensemble-mean epoch differences in surface air temperature for all ensembles (Figure S2). The dominant mode (Figure S2a) explains 40% of the variance in inter-model temperature changes, and the spatial structure strongly resembles the pattern of ensemble-mean temperature association with the ΔSST change (Figure 2b). Most notably, Mode 1 shows similar western Pacific cooling, North Pacific/North American and North Atlantic warming as the Δ_Δ correlation map (Figure S2a vs. 2c). Furthermore, PC1 is significantly correlated with the set of ensemble mean changes in Δ_Δ (Figure S2b). This indicates that there is indeed a large-scale pattern of inter-model differences which is systematically associated with differences in Δ_Δ. Interestingly, the equatorial signal is dominated by western Pacific cooling, rather than eastern Pacific warming; the precise reasons for this are beyond the scope of the present study, but may relate to a larger thermodynamic sensitivity of the warm pool to global-mean temperature changes (e.g. (*15*)).

We note that there also appears to be some contribution from Mode 2 of inter-model spread to the spread in Δ_Δ (Figure S2c). In Mode 2, warming is especially pronounced in the eastern Pacific and the tropical Atlantic. The PC of this mode is also significantly correlated with Δ_Δ (Figure S2d). We hypothesize that these two modes may relate to the differing effects of greenhouse gas and aerosol forcing on patterns of temperature change (not pictured). This could not be definitively proved owing to the lack of sufficient numbers of single-forcing Large Ensembles extending through the end of the 21st century, and is thus beyond the scope of this study. However, the spatial similarity between Figure 2 and Modes 1 and 2 of inter-model spread, as well as the significant cross-ensemble correlation of the inter-model spread PCs with Δ_Δ (p-value <0.1; Figure S2b,d), suggest that the SST gradient is sensitive to inter-model physical differences which produce coherent spatial patterns in their responses to forcing.

4 Historical Patterns Associated with SST Gradient Sensitivity

Another powerful feature of the ensemble-mean regression technique is the ability to relate future changes to the simulated historical climate. This technique enables the identification of aspects of present-day climate with potential predictive power in determining future changes associated with the SST gradient. Figure 2a and c correlate 21st century - 20th century differences in gridpoint circulation changes with Δ_Δ for all ensembles. Once again, coherent patterns emerge: models with larger Δ_Δ show higher historical precipitation throughout the North and South Pacific subtropics/midlatitudes, as well as the Atlantic, and drying occurs in the Indian Ocean. Models with higher Δ_Δ also exhibit strong precipitation increases near the climatological locations of the Intertropical Convergence Zone (ITCZ) and South Pacific Convergence Zone (SPCZ). High 500 hPa heights over the Tibetan Plateau are associated with large Δ_Δ, with a wavetrain-like signature present over the midlatitude North Pacific suggestive of anomaly propagation from the Tibetan Plateau region (Figure 2c). Interestingly, historical ocean temperatures in most locations are not significantly correlated with Δ_Δ (Figure 2a) - but land temperatures have a strong relationship over the majority of the land surface. The magnitude of the correlation is particularly strong over midlatitude Eurasia and North America (Figure 2a), suggesting a possible role for coupling with the land surface.

The presence of systematic historical mean-state differences between models with high versus low Δ_Δ is further confirmed by separating models into populations based on their Δ_Δ values (Methods). In the eastern Indian Ocean, historical precipitation is significantly lower in models with higher Δ_Δ (Figure 2e). In contrast, in the central Pacific, models with higher Δ_Δ show larger historical precipitation along the equator and a tendency for reduced off-equatorial precipitation indicative of a southward ITCZ shift (Figure 2f). The spatial patterns of historical mean-state differences between high- and low-Δ_Δ models (Figure S3a,b) also bear a strong resemblance to those of Figure 2. Higher-Δ_Δ models have higher historical air temperatures over land (Figure S3a), particularly over Eurasia and northern Africa. The precipitation patterns in the tropics also show a tendency for drier historical conditions over the Indian Ocean and Maritime Continent, with enhanced rainfall over the western/central Pacific (Figure S3b).

We note that there is some seasonal dependence of these results. The higher historical eastern Pacific temperatures in high-Δ_Δ models are more pronounced during JJA (Figure S3e), but the historical land surface temperature is slightly larger during DJF (Figure S3c). The precipitation patterns differ slightly as well, with the subtropical Indian Ocean showing drier historical precipitation during DJF (Figure S3b) and wetter historical conditions over the Indian subcontinent during JJA in high-Δ_Δ models (Figure S3d). This difference may relate to influences on the Indian summer monsoon, and potentially also to connections with the Indian Ocean Dipole, which peaks in boreal autumn (*26*). We primarily focus on the temperature associations over the Northern Hemisphere land masses and the precipitation associations over the equatorial Pacific, which are robust features of high-Δ_Δ models across all seasons.

5 Cloud Radiative Impacts on Inter-Model Spread

5.1 All Models

Section 4 demonstrates the clear connection between inter-model spread in historical mean climate and Δ_Δ, which likely reflects a systematic dependence of atmosphere/ocean feedbacks on mean climate. To further explore this possibility, we calculate the regression of gridpoint net surface shortwave radiation on SST anomalies, where anomalies are calculated relative to the seasonal cycle and the ensemble mean is removed from each member prior to analysis (Figure 3). These regressions are computed over the time dimension for individual ensemble members, then the ensemble mean for each model/scenario combination is averaged, then the ensemble means are averaged together to form the maps in Figure 3. Here these calculations roughly follow the 'cloud-shortwave feedback index' approach of (*7*), which was shown to effectively indicate the influence of cloud feedbacks on the SST pattern responses to anthropogenic warming.

In the tropical oceans, a negative regression coefficient between surface net shortwave flux and SSTA (SW:SSTA) indicates that local warming increases cloud cover (and decreases surface shortwave radiative flux), which is generally true in regions dominated by deep convection (see Figures S4, S5). Negative coefficients can be seen in cumulus-dominated regions such as the western Pacific warm pool and the tropical Atlantic, and zonal bands of negative coefficients are also present near the climatological locations of the ITCZ and SPCZ (Figure 3a). Interestingly, the negative coefficients near 5-10°N do not fully persist across the basin in the multi-model mean (Figure 3a), where coefficients become smaller or positive for longitudes east of roughly 150°W. This may reflect either the presence of stratiform rain within the ITCZ (e.g. (*27,28*)), or the diversity of representation of the ITCZ location and strength across models (Figure S5). In contrast, positive SW:SSTA coefficients are present in stratus regimes of the far eastern equatorial Pacific, where SST increases lead to reduced cloud cover and increased surface shortwave radiation.

There is overall low inter-model agreement on the sign of the regression coefficients in the equatorial Pacific (Figure 3a). The multi-model ensemble-mean value is generally negative west of 160°W and positive eastwards, but less than 2/3 of models agree on the sign at any given longitude. This disagreement is an indication of the large spatial diversity of the feedback patterns across models (see also Figure S5). To assess the importance of this inter-model diversity in generating spread in future projections, we apply another ensemble-mean regression: a regression of the SW:SSTA coefficients of Figure 3a on the SST gradient sensitivity for each model/scenario combination. There is a large negative association near 160-200°E along the equator, with a positive association immediately to its west (Figure 3e). This suggests that models where the historical location of deep convection is shifted farther to the east (or with overall stronger deep convection) are also those which experience a stronger future weakening of ΔSST.

The sign transition near 140E in Figure 3a coincides approximately with the climatological edge of the western Pacific warm pool (green contour). The western Pacific also generally tends to be the location where the equatorial sensitivity of precipitation to SST anomaly is largest, as measured by the regression of gridpoint precipitation anomaly onto local SSTA (Figure S6). Near the warm pool edge, variations in local SSTA are most effective at exciting deep convection, as indicated by both the negative SW:SSTA feedback and the increase in precipitation sensitivity to SST (e.g. (*9, 29*); see also Figure S7). Additionally, differencing the precipitation:SST anomaly regression coefficients between high and low Δ_Δ models shows that high-Δ_Δ models have more positive precipitation responses to SSTA in the central Pacific over the 20th century (Figure S7).

Our proposed mechanism linking the feedbacks above with future SST gradient responses is as follows (Figure 4). In models with historically stronger precipitation over the central equatorial Pacific, the negative SW:SSTA feedback will be larger in the central/western Pacific, since a smaller increase in SSTA is required to initiate additional convective precipitation in this region. (In the eastern equatorial Pacific, the SST lies generally below the threshold for deep convection, and stratiform clouds with positive SW:SSTA feedback are favored.) The negative feedback in the central/western Pacific will tend to suppress local CO_2-induced warming there, and induce an *anomalous* lack of further convection. The resulting anomalous atmospheric descent operates essentially as the inverse of the classical (*30*) response to surface heating: descending air near the dateline will tend to diverge at the surface and induce a westerly wind anomaly in the eastern Pacific. This then reduces the trade wind strength and leads to further warming of the eastern Pacific, favoring the development of an El Nino-like reduction in the SST gradient.

The above mechanism is conceptually similar to that proposed by (*7*), who proposed that systematic underestimates in the strength of SW:SSTA feedbacks should cause erroneous surface convergence and cause models to simulate overly La Nina-like responses to greenhouse gas increases. Here, we show that models with high Δ_Δ behave in essentially the opposite fashion: when convection is stronger, surface divergence favors El Nino-like warming.

5.2 Wet Models

It is important to note that the relationships shown in Figure 3 appear to change in models with extremely high climatological-mean equatorial precipitation (Methods). In these models (hereafter the 'wet' models; Table S4), the negative SW:SSTA relationship is markedly enhanced (Figure 3b). However, the magnitude of this feedback decreases in the future (Figure 3d), whereas for models as a whole the tendency is for a slight increase (Figure 3c). This suggests that for the wettest models, the central Pacific divergent surface wind mechanism may be expected to weaken by the late 21st century. The pattern of SW:SSTA regressions associated with Δ_Δ also differs in wet models (Figure 3f), with much larger negative signals over the far western Pacific and larger positive signals over the far eastern Pacific.

We hypothesize that this regime transition relates to the 'saturation' of atmospheric convection at high SST values. Wet models generally begin with warmer SSTs in the eastern Pacific over the 20th century (Figure S8), and also exhibit a systematically lower threshold SST at which deep convection is initiated (Figure 5a; Methods). This means that a higher proportion of the tropical ocean exceeds the convective threshold in these models (Figure 5c). However, the exceedance fraction in wet models is *less* likely to increase in the future (Figure 5e vs 5d), since SSTs are already sufficiently warm in the 20th century for convection to be commonplace. This effect can be observed both for wet models as compared with dry models (Figure 5e), as well as within the population of wet models (Figure S9).

The mechanism driving this behavior for the wet models is summarized in Figure 4c,d. Initially large central equatorial Pacific cloud shading drives a divergent wind response, as is the case for the full population of models. However, because the wet models have warmer eastern Pacific SSTs (Figure S8), deep convection can initiate in the eastern portion of the basin. Eastern Pacific deep convection will then lead to a larger negative shortwave feedback, creating a direct suppression of further warming. As is the case for colder models, this suppression of warming can also create an anomalous descent: however, since the surface divergence is now centered farther east, it acts to increase the equatorial trades, and therefore leads to a less El Niño-like warming pattern.

This framework is also consistent with the SST gradient:SW feedback regression pattern in Figure 3f. For the wet models, El Niño-like warming is enhanced when the eastern Pacific feedback is more positive. However, in the very wettest models the *negative* feedback is enhanced (Figure S9), therefore resulting in a less El Niño-like SST gradient trend. Likewise, the wettest models also have a less negative feedback in the far western Pacific, again tending to oppose El Niño-like future changes.

6 Implications for Constraining Future Projections

The concept of ‘emergent constraints’ based on historical observations which can be used to predict the reliability of future projections has recently been applied in various contexts, including equilibrium climate sensitivity, global-mean temperature, and runoff (*31–33*). The strong relationship between historical convective precipitation and Δ_Δ suggests that this framing may also be useful here. Motivated by Figure 2, we relate Δ_Δ to the historical mean precipitation in the central Pacific (5°S-5°N, 150°E-150°W; Figure 6a). This region is chosen since it coincides with the large correlation between Δ_Δ and historical precipitation in Figure 2d. The fits in Figure 6 are performed using a spline polynomial, since the sign of the relationship reverses for historical precipitation values greater than roughly 4.5 mm/day. This results in improved estimates of explained variance relative to a simple linear regression (not pictured). The fitted relationship is highly statistically significant, and the observations lie within the spread of the models. However, both the GPCP and CMAP estimates are on the high end of the simulated values, suggesting that many models tend to underestimate historical precipitation in this region (see also Figure S10). This is also consistent with the known cold-tongue bias in coupled models, which suppresses deep convection in the central equatorial Pacific (*5*).

The fact that the observational estimates of precipitation coincide with the reversal of the precipitation:Δ_Δ relationship in Figure 6 is notable. This study cannot determine the precise reasons for this correspondence, which is left for future work. However, we note that a threshold of 5 mm/day for equatorial Pacific precipitation has been previously shown to be appropriate for identifying large-scale convective reorganization (*9, 34, 35*). This provides a physical explanation for the existence of the inflection point in Figure 6, and suggests that such a relationship may truly exist in nature.

Since observations by necessity contain only a single realization, a more fair model/observational comparison uses individual ensemble member estimates. This is shown in Figure 6b: the scatter is of course larger, but the historical-future relationship remains statistically significant and the explained variance is nearly identical (not pictured). The distinct downward tendency in the relationship at higher precipitation values is clearly apparent, although we note that this is dominated by simulations using MIROC6 and MIROC-ES2L (Figure 6b). Nonetheless, the statistical significance of this relationship implies that it may be useful as a true emergent constraint on model projections. We have applied this constraint in Figure 6c, by selecting all ensemble members where the mean precipitation over 1979-2024 falls between the estimates from GPCP and CMAP; the distribution of Δ_Δ values in these members are then plotted. The peak of the distribution lies roughly at a gradient change value of 0.2°C/degree C global warming, which should be expected to be the 'true' change if this relationship holds in nature.

7 Discussion and Conclusions

The effect of future climate change on the east-west gradient in equatorial Pacific SST (ΔSST) is of fundamental importance for improving projections of weather extremes and ecosystem impacts, yet physical differences among models and internally generated climate variability has made it difficult to determine why models project such different futures. Here we have leveraged the power of combining many Large Ensembles to gain insight into the mechanisms underlying inter-model spread in ΔSST. This is an analysis which was not possible to perform even a few years ago - it is only through the combination of many Large Ensembles with differing model physics that one can robustly examine changes in the forced response. The results demonstrate the presence of coherent patterns in atmospheric conditions associated with inter-model SST gradient sensitivity (Δ_Δ; the change in the east-west equatorial SST temperature difference, normalized to global-mean temperature change), which also strongly resemble the dominant modes of inter-model temperature spread diagnosed via EOF analysis. This implies that Δ_Δ is a robust feature of inter-model circulation differences.

A crucial aspect of our results is the ability to relate Δ_Δ and the representation of historical climate. El Nino-like future SST gradient reductions are preferentially associated with larger historical precipitation in the central equatorial Pacific, and smaller precipitation over the Indian Ocean. Enhanced land surface warming is also associated with high Δ_Δ - warming appears across the majority of the Northern Hemisphere land area, particularly over Eurasia.

The historical representation of equatorial deep convection seems to drive the emergent behavior of the SST gradient, through modifying the strength of equatorial shortwave:SST feedbacks. Central Pacific feedbacks generally dominate: in models where the location of deep convection is shifted farther east and/or the magnitude of convection is stronger near the dateline, the negative feedback between SSTA and net shortwave flux is larger. This will tend to suppress greenhouse gas-induced warming, leading to a relative cool anomaly near the dateline. The associated anomaly in atmospheric convection is toward vertical descent and surface wind divergence, a Gill-type response to a relative lack of tropical convection (*30*). In the eastern part of the basin, the net effect is a weakening of the equatorial trade winds and an eastward migration of SST anomalies: in other words, these models are primed to favor more El Nino-like future changes.

The above mechanism is modified in models for which the central equatorial Pacific precipitation $\geq$ 4.5 mm/day (the ‘wet’ models). In these models, stronger historical precipitation leads to a less El Niño-like pattern. This relates to the initial very strong negative shortwave feedback, which extends across much of the Pacific. As convection shifts into the eastern portion of the basin, the negative feedback weakens dramatically in the western Pacific and strengthens in the east. The result is a tendency for the trade winds to increase slightly relative to other ‘wet’ models, due to a combination of direct radiative cooling from increased Eastern Pacific cloud cover and the eastward-shifted location of the surface divergent wind response.

We have used the historical:future climate relationships emerging from the Large Ensembles to identify possible observable emergent constraints on Δ_Δ. The historical magnitude of central equatorial Pacific precipitation shows a highly robust relationship with Δ_Δ, with wetter models producing more El Niño-like future changes. Crucially, this relationship is present both among ensemble-mean and ensemble-member values, and allows for direct comparison with values estimated from historical observations. However, the relationship is nonlinear - for the wettest models, the sign of the relationship reverses due to the changes in feedback structure mentioned above.

The inflection point in this emergent constraint relationship occurs close to the observed value of historical precipitation, suggesting that whether models under- or overestimate precipitation, they tend to be insufficiently El Niño-like in their future SST gradient projections. The majority of models underestimate central equatorial Pacific precipitation, and therefore our results would predict that they also underestimate El Niño-like warming. For the wet models which overestimate precipitation, given the negative sign of the relationship for that parameter space, the emergent constraint relation would also indicate that those models should project a more El Niño-like change. In other words, future projections "should" be even more El Nino-like. We note some caveats to this statement: for instance, recent work has highlighted models' tendency to simulate *overly* El Nino-like trends compared with observations (*11*), but the past 40 years are known to be influenced by both greenhouse gas and aerosol emissions. Additionally, recent high-resolution simulations with the Community Earth System Model (CESM1) show an increased level of agreement with observational trends (*36*). We hypothesize that there may be other processes missing in models, which could generate additional errors - a full accounting is beyond the scope of the present study, but one example might be small-scale ocean variability (e.g. mesoscale eddies/tropical instability waves). The behavior of the mean thermocline may also play a role, but could not be analyzed here owing to limitations in data availability.

These results have important implications for the accuracy of future SST gradient projections. Previous work has suggested that models may simulate overly La Nina-like future SST gradient changes, due to underestimation of the SW:SSTA feedbacks (*7*). Our results are consistent with this picture: the 'high-Δ_Δ' models with more El Nino-like gradient changes are also the models which agree more closely with precipitation observations. However, we caution that the possibility of compensating errors still remains, and that models may be missing additional processes which might create more La Nina-like gradient projections if they were corrected. Nonetheless, this analysis provides a framework for constructing dynamically-based emergent constraints on future tropical Pacific changes - and eventually, possibly a path toward improving the accuracy of future projections.

Acknowledgments

Funding: SS was supported by NSF CAREER, OCE-2142953. CD was supported by the NSF National Center for Atmospheric Research, which is a major facility sponsored by the NSF under the Cooperative Agreement 1852977. NM was supported by the Australian Research Council Discovery Early Career Researcher Award DE230100315. Computing and data storage resources, including the Derecho supercomputer, were provided by the Computational and Information Systems Laboratory at NCAR. We also acknowledge the Community Earth System Model, version 1, Large Ensemble Community Project; the Community Earth System Model, version 2, Large Ensemble Community Project; and the CESM Climate Variability and Change Working Group.

Author contributions: SS conceived the study, performed analyses, and wrote the manuscript. CD contributed to study design. All authors contributed to editing the manuscript.

Competing interests: There are no competing interests to declare.

Data and materials availability: All codes used to perform these analyses are available at:
https://github.com/samanthastevenson/EqPacTrends_SMILES
Data from large ensemble simulations are publicly available via the Glade file system at the NSF National Center for Atmospheric Research.

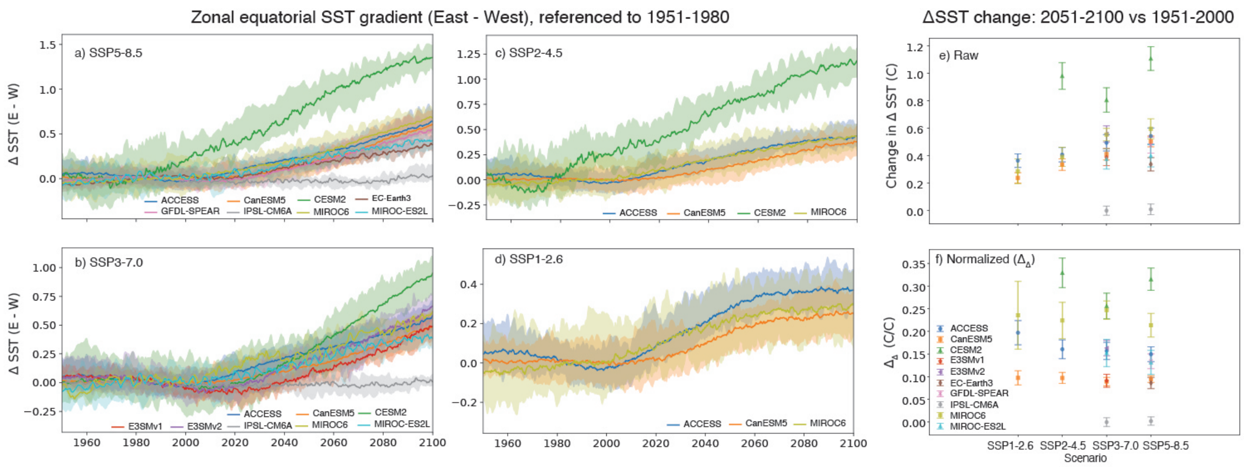

Figure 1: Changes in the SST gradient (Δ SST) in the Pacific. a)-d) 30-year running mean time series of the SST gradient for four different future scenarios: a) SSP5-8.5; b) SSP3-7.0; c) SSP2-4.5; d) SSP1-2.6. Solid lines indicate ensemble median, and colored shading the ensemble min/max range. All gradient values are calculated relative to the ensemble average over the 1951-1980 reference period. e) Epoch-averaged change in the SST gradient, differenced between 2050-2100 and 1950-2000. f) Same as e), but normalized to each model's area-weighted global-mean temperature change between the two averaging periods (Δ_Δ values, as described in the main text).

References and Notes

1. C. F. Ropelewski, M. S. Halpert, Global and regional scale precipitation patterns associated with the El Niño/Southern Oscillation. *Monthly Weather Review* **114**, 2352–2362 (1987).

2. A. S. Taschetto, *et al.*, ENSO atmospheric teleconnections. *El Niño southern oscillation in a changing climate* pp. 309–335 (2020).

3. S. Lee, *et al.*, On the future zonal contrasts of equatorial Pacific climate: Perspectives from Observations, Simulations, and Theories. *Npj Climate and Atmospheric Science* **5** (1), 82 (2022).

4. G. Vecchi, B. Soden, Global Warming and the Weakening of the Tropical Circulation. *Journal of Climate* **20**, 4316–4340 (2007), doi:10.1175/JCLI4258.1.

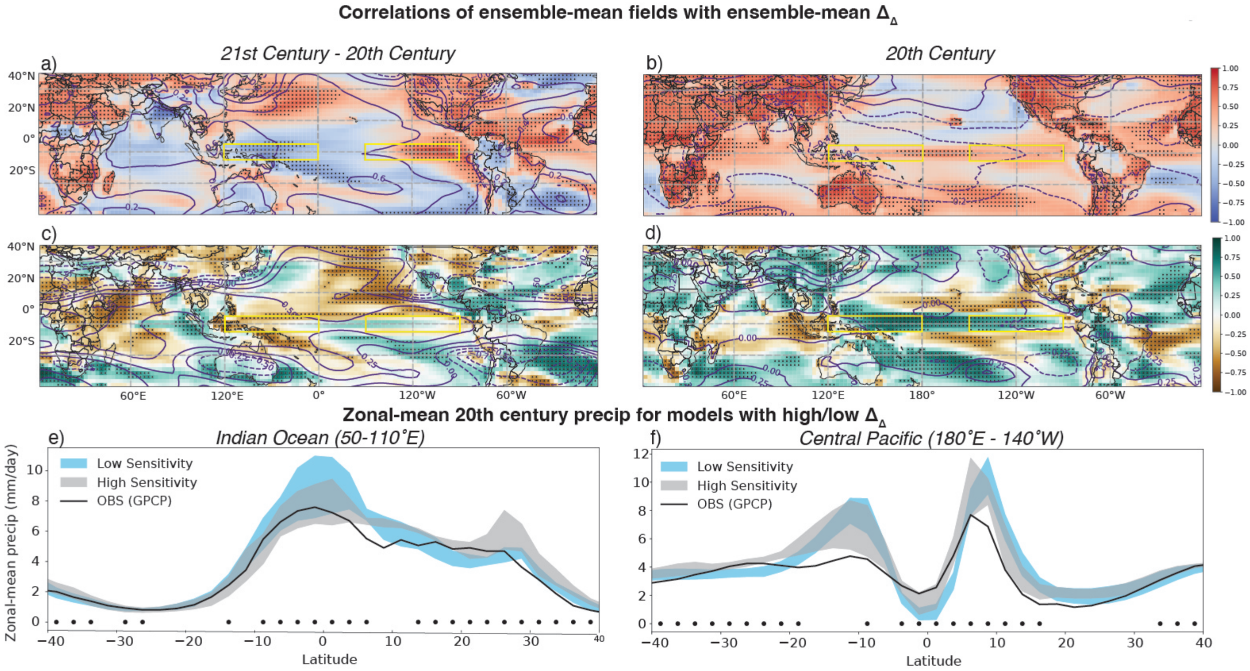

Figure 2: Large-scale circulation patterns associated with Δ_Δ spread across models. a) Correlation of ensemble-mean gridpoint 21st century - 20th century surface temperature (colors) and sea level pressure (contours) differences with the ensemble-mean Δ_Δ, across the collection of all ensemble means for each model/scenario combination. b) Correlation of ensemble-mean gridpoint 20th century surface temperature (colors)/SLP (contours) with Δ_Δ. c) Same as a), but correlations are performed between gridpoint precipitation (colors) or 500 hPa geopotential height (contours) and Δ_Δ. d) Same as b), but correlations are performed between gridpoint precipitation (colors) or 500 hPa geopotential height (contours) and Δ_Δ. The time-varying global mean is removed from the geopotential height maps prior to regression, to better isolate the spatial pattern. All time differences are calculated between 2050-2099 and 1951-1999, and stippling indicates differences significant at 90% using a Wilcoxon rank-sum test. e) Zonal-mean precipitation averaged over the Indian Ocean (50-110°E), for models with high versus low Δ_Δ values. f) Same as e), but for precipitation averaged over the central Pacific (180-220°E). Black dots in e), f) indicate latitudes where the high and low sensitivity models differ significantly at the 90% level using a Wilcoxon rank-sum test. Black solid lines in e), f) show observationally averaged values from the GPCP dataset.

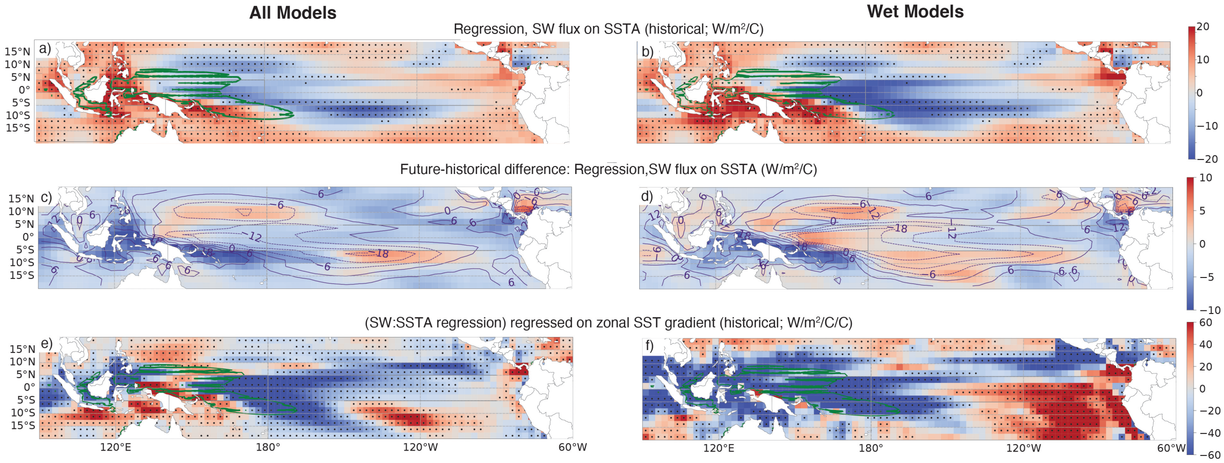

Figure 3: Cloud shortwave feedback relationships for a), c), e) the set of all ensembles and b), d), f) the set of all ensembles where central equatorial Pacific historical mean precipitation exceeds 4.5 mm/day. a, b) Multi-model ensemble mean of historical gridpoint regression coefficients for net shortwave flux regressed onto local SST anomaly (regressions computed individually for each ensemble member, averaged over the ensemble, then the multi-ensemble average computed). Green contour indicates the multi-model ensemble mean climatological location of the 28°C isotherm. c), d) Differences between the future - historical SW:SSTA regression coefficient (colors) and the historical values (contours). e, f) Regression of the SW:SSTA regression coefficient in a) onto Δ_Δ (stippling indicates locations where regression is significant at the 90% level). Stippling in a),b) indicates locations where 2/3 of model/ensemble combinations agree on the sign of the regression coefficient.

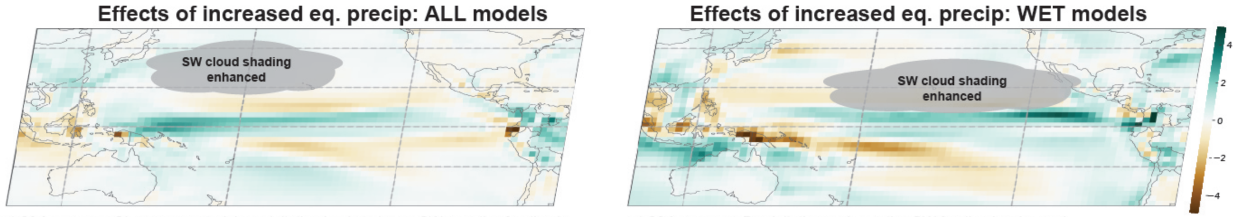

a) **20th century**: Stronger equatorial precipitation leads to larger SW negative feedback

c) **20th century**: Precipitation and negative SW feedback enhanced throughout equatorial region

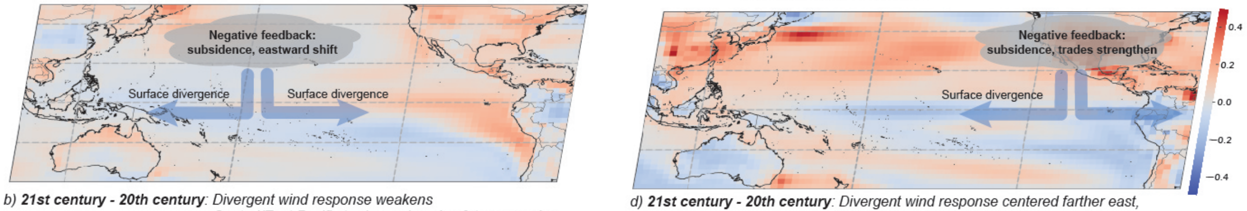

b) **21st century - 20th century**: Divergent wind response weakens Central/East Pacific trades, enhancing future warming

d) **21st century - 20th century**: Divergent wind response centered farther east, enhances trades; SST gradient reduced

Figure 4: Schematic illustrating the proposed mechanism for El Nino-like ΔSST changes in response to future warming. a) Colors indicate ensemble mean precipitation differences between high and low SST Δ_Δ models (mm/day) over the 20th century. b) Colors indicate ensemble mean temperature differences between the future and 20th century, differenced between high and low Δ_Δ models (C). c) Same as a), for differences between sets of wet models: (MIROC6, MIROC-ES2L) - (CESM2, E3SMv2). d) Same as b), for differences between (MIROC6, MIROC-ES2L) and (CESM2, E3SMv2).

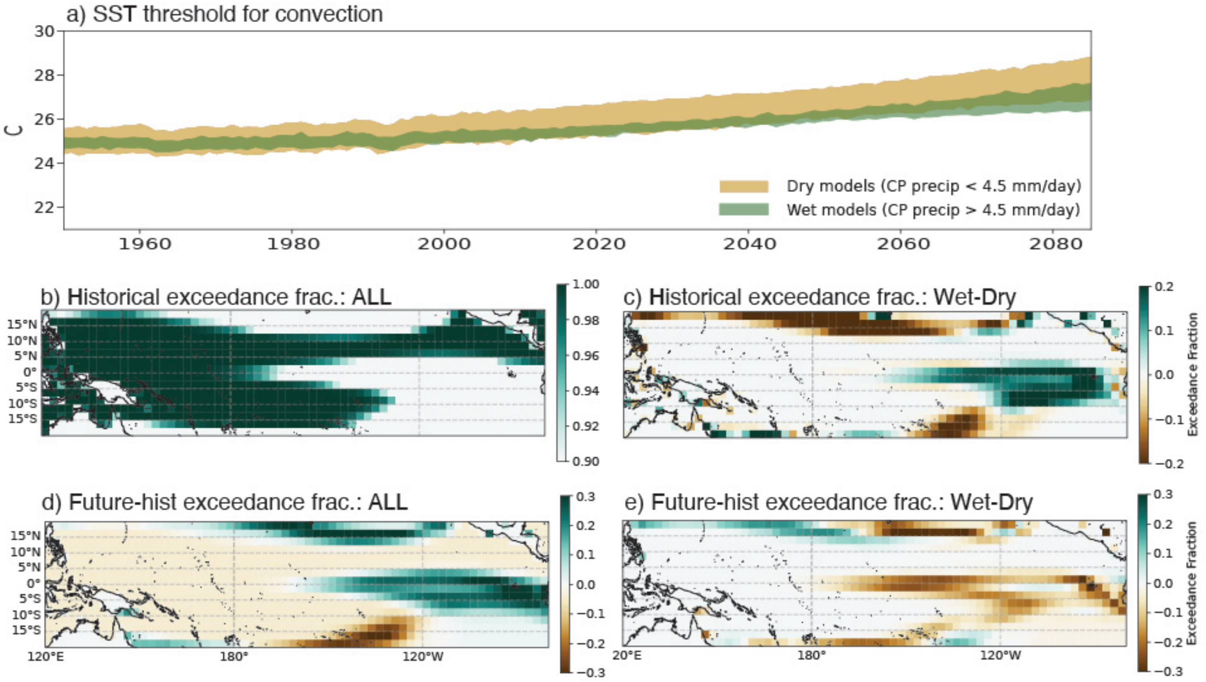

Figure 5: Convective threshold behaviors. a) Time series of the SST threshold for deep convection (tropical precipitation ≥ 2 mm/day), for the 'dry' and 'wet' subsets of model ensembles. b) Multi-model ensemble mean convective threshold exceedance fraction, averaged over the 20th century. c) Difference between convective threshold exceedance fraction, for the wet vs dry models. d) Difference between the multi-model ensemble mean exceedance fractions, between the future and 20th centurys. e) Difference between the future-historical exceedance fraction differences, between the wet and dry model subsets.

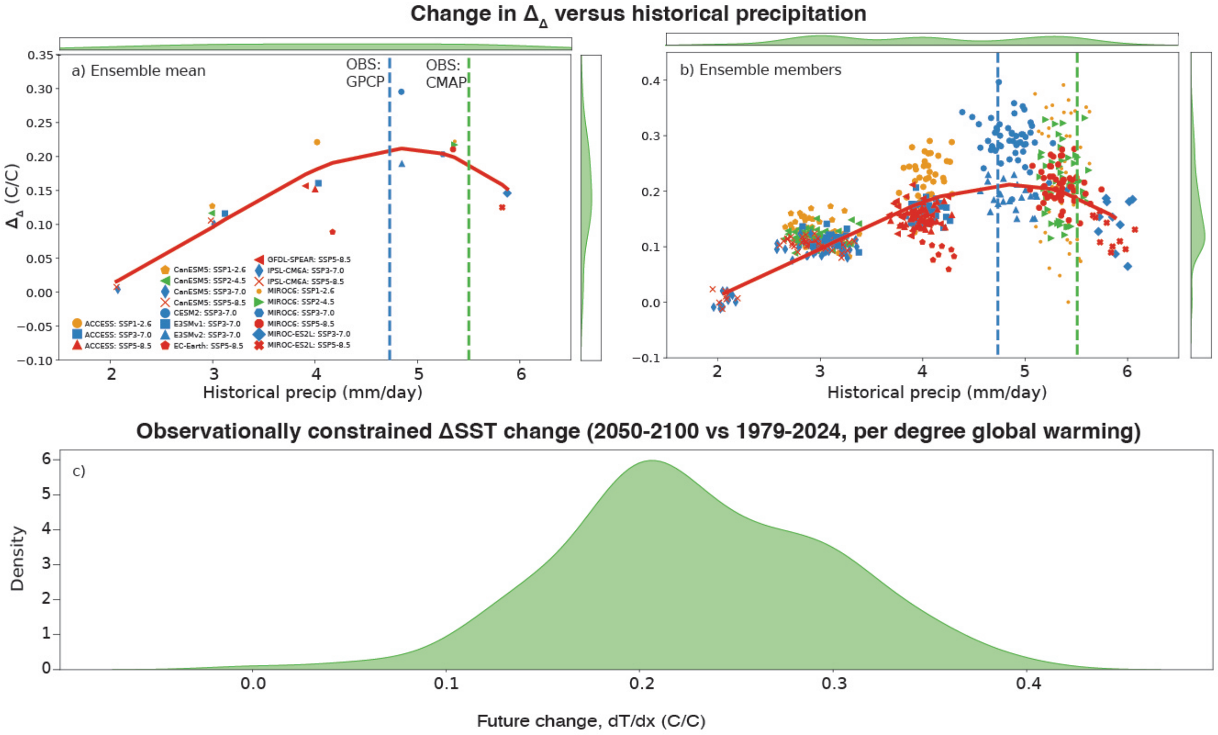

Figure 6: A proposed emergent constraint on ΔSST. The Δ_Δ value is plotted versus the historical average of central Pacific precipitation (5°S-5°N, 150°E - 150°W). Here the 20th century is defined as 1979-2024 to maximize overlap with observations, and the future period is defined as 2050-2100. Vertical dashed lines indicate the historical precipitation changes derived from observations: GPCP (blue) and CMAP (green). Solid lines of best fit are plotted in red, calculated using a third-degree polynomial spline. Plots along x- and y-axes of a) and b) indicate kernel density estimate (KDE) fits to the distribution of precipitation (x-axis) and temperature gradient change (y-axis). c) Emergent constraint applied to ensemble-member estimates. All ensemble members in b) where historical (1979-2024) precipitation falls between the GPCP and CMAP estimates are selected, then the KDE for the corresponding Δ_Δ over (2050-2100) - (1979-2024) values is constructed.

5. H. Bellenger, E. Guilyardi, J. Leloup, M. Lengaigne, J. Vialard, ENSO representation in climate models: from CMIP3 to CMIP5. *Climate Dynamics* (2014), dOI:10.1007/s00382-013-1783-z.

6. E. Guilyardi, A. Capotondi, M. Lengaigne, S. Thual, A. T. Wittenberg, ENSO modeling: History, progress, and challenges. *El Niño Southern Oscillation in a changing climate* pp. 199–226 (2020).

7. J. Ying, P. Huang, Cloud?Radiation Feedback as a Leading Source of Uncertainty in the Tropical Pacific SST Warming Pattern in CMIP5 Models. *Journal of Climate* **29**, 3867–3881 (2016), dOI: 10.1175/JCLI-D-15-0796.1.

8. J. Ying, P. Huang, The Large-Scale Ocean Dynamical Effect on Uncertainty in the Tropical Pacific SST Warming Pattern in CMIP5 Models. *Journal of Climate* **29**, 8051–8065 (2016), dOI: 10.1175/JCLI-D-16-0318.1.

9. S. Stevenson, A. T. Wittenberg, J. Fasullo, S. Coats, B. Otto-Bliesner, Understanding diverse model projections of future extreme El Niño. *Journal of Climate* **34** (2), 449–464 (2021).

10. R. Seager, N. Henderson, M. Cane, Persistent discrepancies between observed and modeled trends in the tropical Pacific Ocean. *Journal of Climate* **35** (14), 4571–4584 (2022).

11. R. C. Wills, Y. Dong, C. Proistosecu, K. C. Armour, D. S. Battisti, Systematic climate model biases in the large-scale patterns of recent sea-surface temperature and sea-level pressure change. *Geophysical Research Letters* **49** (17), e2022GL100011 (2022).

12. I. Held, B. Soden, Robust Responses of the Hydrological Cycle to Global Warming. *Journal of Climate* **19**, 5686–5699 (2006), doi:10.1175/JCLI3990.1.

13. M. F. Stuecker, *et al.*, Strong remote control of future equatorial warming by off-equatorial forcing. *Nature Climate Change* pp. 1–6 (2020).

14. T. R. Knutson, S. Manabe, Time-mean response over the tropical Pacific to increased CO_2 in a coupled ocean-atmosphere model. *Journal of Climate* **8**, 2181–2199 (1995).

15. A. C. Clement, R. Seager, M. A. Cane, S. E. Zebiak, An ocean dynamical thermostat. *Journal of Climate* **9**, 2190–2196 (1996).

16. N. Maher, *et al.*, The updated Multi-Model Large Ensemble Archive and the Climate Variability Diagnostics Package: New tools for the study of climate variability and change. *EGUsphere* **2024**, 1–28 (2024).

17. J. E. Kay, *et al.*, The Community Earth System Model (CESM) Large Ensemble Project: A Community Resource for Studying Climate Change in the Presence of Internal Climate Variability. *Bulletin of the American Meteorological Society* (2015), doi:10.1175/BAMS-D-13-00255.1.

18. C. Deser, *et al.*, Isolating the evolving contributions of anthropogenic aerosols and greenhouse gases: A new CESM1 large ensemble community resource. *Journal of climate* **33** (18), 7835–7858 (2020).

19. N. Maher, *et al.*, The future of the El Niño-Southern Oscillation: Using large ensembles to illuminate time-varying responses and inter-model differences. *Earth System Dynamics Discussions* pp. 1–28 (2022).

20. H.-B. Fredriksen, J. Berner, A. C. Subramanian, A. Capotondi, How does El Niño–Southern Oscillation change under global warming—A first look at CMIP6. *Geophysical Research Letters* **47** (22), e2020GL090640 (2020).

21. P. N. DiNezio, A. C. Clement, G. A. Vecchi, S.-K. Lee, Climate Response of the Equatorial Pacific to Global Warming. *Journal of Climate* **22**, 4873–4892 (2009), dOI:10.1175/2009JCLI2982.1.

22. G. A. Meehl, *et al.*, Context for interpreting equilibrium climate sensitivity and transient climate response from the CMIP6 Earth system models. *Science Advances* **6** (26), eaba1981 (2020).

23. M. D. Zelinka, *et al.*, Causes of higher climate sensitivity in CMIP6 models. *Geophysical Research Letters* **47** (1), e2019GL085782 (2020).

24. I. R. Simpson, *et al.*, The CESM2 single-forcing large ensemble and comparison to CESM1: Implications for experimental design. *Journal of Climate* **36** (17), 5687–5711 (2023).

25. B. C. O'Neill, *et al.*, The Scenario Model Intercomparison Project (ScenarioMIP) for CMIP6. *Geosci. Model Dev.* **9**, 3461–3482 (2016).

26. N. H. Saji, B. N. Goswami, P. N. Vinayachandran, T. Yamagata, A dipole mode in the tropical Indian Ocean. *Nature* **401**, 360–363 (1999).

27. C. Schumacher, R. A. Houze, Stratiform rain in the tropics as seen by the TRMM precipitation radar. *Journal of Climate* **16** (11), 1739?1756 (2003).

28. L. Huaman, C. Schumacher, Assessing the vertical latent heating structure of the East Pacific ITCZ using the CloudSat CPR and TRMM PR. *Journal of Climate* **31** (7), 2563–2577 (2018).

29. M. Watanabe, A. T. Wittenberg, A method for disentangling El Niño-mean state interaction. *Geophysical Research Letters* **39**, L14702 (2012), doi:10.1029/2012GL052013.

30. A. E. Gill, Some simple solutions for heat induced tropical circulation. *Q. J. R. Meteorol. Soc.* **106**, 447–462 (1980).

31. P. M. Caldwell, M. D. Zelinka, S. A. Klein, Evaluating emergent constraints on equilibrium climate sensitivity. *Journal of Climate* **31** (10), 3921–3942 (2018).

32. K. B. Tokarska, *et al.*, Past warming trend constrains future warming in CMIP6 models. *Science advances* **6** (12), eaaz9549 (2020).

33. F. Lehner, *et al.*, The potential to reduce uncertainty in regional runoff projections from climate models. *Nature Climate Change* **9**, 926–933 (2019).

34. W. Cai, *et al.*, Increasing frequency of extreme El Nino events due to greenhouse warming. *Nature Climate Change* **4**, 111–116 (2014), doi:10.1038/NCLIMATE2100.

35. W. Cai, *et al.*, Increasing frequency of extreme La Nina events due to greenhouse warming. *Nature Climate Change* **5**, 132–137 (2015), doi:10.1038/nclimate2492.

36. P. Chang, *et al.*, An unprecedented set of high-resolution earth system simulations for understanding multiscale interactions in climate variability and change. *Journal of Advances in Modeling Earth Systems* **12** (12), e2020MS002298 (2020).